DOE/ET-53088-296 IFSR #296

Saturation of Kelvin-Helmholtz Fluctuations in a Sheared Magnetic Field

Bruce D. Scott, P. W. Terry, and P. H. Diamond

Institute for Fusion Studies
University of Texas at Austin
Austin, Texas 78712

August 1987

Saturation of Kelvin-Helmholtz Fluctuations in a Sheared Magnetic Field

Bruce D. Scott, P. W. Terry, and P. H. Diamond

Institute for Fusion Studies, University of Texas, Austin, TX 78712

ABSTRACT

Kelvin-Helmholtz unstable flows are numerically investigated in the context of a sheared $\mathbf{E} \times \mathbf{B}$ flow profile and a sheared magnetic field in the collisional, electrostatic limit. In the extreme form of this limit, density fluctuations are small, and the system is described by the nonlinear $\mathbf{E} \times \mathbf{B}$ vorticity dynamics. In order to focus on the role of magnetic shear localisation, the computations are confined to two dimensions. For weak magnetic shear the fluctuations become turbulent and saturate by nonlinear cascade to small (dissipative) scales. In a strong magnetic shear regime near the linear stability boundary, nonlinear spatial broadening allows direct access to resistive shear dissipation, leading to saturation at small amplitude with nearly all the fluctuation energy in the longest-wavelength mode. This is in accordance with previous investigation using a statistical closure analysis [*Phys. Fluids* **29**, 231 (1986)]. The amount of broadening is proportional to the linear growth rate. The fluctuation amplitude scaling with magnetic shear is found to agree closely with the theory.

I. Introduction

The phenomenon of the Kelvin-Helmholtz instability is generally well known.[1] The velocity gradient serves as an energy source, provided it is externally maintained. Small perturbations whose wavelength along the equilibrium flow is longer than the shear layer width will grow to finite amplitude. In a plasma described by incompressible 2D MHD (magnetohydrodynamics) with a uniform magnetic field placed such that the flow gradient, flow, and magnetic field directions are mutually perpendicular, the result is the same. The field is simply convected around, its magnitude unchanging. However, if the magnetic field has a small, sheared component in the flow direction, the velocity perturbations will only be unstable if $(v_0/v_A) \gtrsim (\Delta_E/L_s)$. In this expression, v_0 and v_A are the shear flow magnitude and Alfvén velocity and Δ_E and L_s are the velocity shear layer width and the magnetic field shear length, respectively. [This is a generalisation of the instability condition $(v_0 > v_A)$ in the event a uniform magnetic field is aligned with the velocity.[1]] Supposing the sheared velocity is not strong enough to overcome field line bending, perturbations can still grow if the plasma is sufficiently *resistive*. That is, if the perturbed flow can slip past the field lines without perturbing them, the free energy in the sheared flow need only overcome resistive shear dissipation. It is with this situation that the present paper is concerned.

Electrostatic potential fluctuations have been observed at the edge of tokamak plasmas for many years.[2–4] These are related to fluctuations in the plasma density, although the respective amplitudes often have differing radial profiles. The density and potential fluctuations are generally of the same order, $\widetilde{n}/n \sim e\widetilde{\phi}/T$, but are not necessarily equal. Equality would indicate an adiabatic electron response, but the collisional conditions result in a substantial if not dominant nonadiabatic character. This is due to the ineffectiveness of parallel dissipation in forcing energy equipartition before the

electrons react to the wave frequencies, typically on the order of the diamagnetic frequency, ω_*. "Collisional conditions" mean that $\omega_* \nu_e > k_\parallel'^2 \Delta_C^2 V_e^2$, where $k_\parallel$ is the parallel wavenumber, Δ_C is the radial correlation length of the fluctuations, and V_e is the electron thermal velocity. [The plasma, however, is not so collisional that perpendicular viscosity is strong enough to force adiabaticity, since $(\nu_e/\omega_*)(m_e/M_i) < 1$.] An "adiabaticity index" (defined by $\Delta_C^2 k_\parallel'^2 V_e^2/\omega_* \nu_e \equiv \Delta_C^2/\Delta_D^2$, where the "$D$" stands for electron dissipation) has recently been found to be of order or less than unity in TEXT edge fluctuation experiments,[5] indicating moderate to strong nonadiabatic electron behaviour.

In addition to the fluctuations, a strongly sheared radial electric field has also been observed in the TEXT edge.[6] This is characterised by a strongly peaked $\mathbf{E} \times \mathbf{B}$ vorticity maximum (width of order 1 cm) located just inside the limiter. The field is as large as 30 V/cm, so assuming a pressure gradient of 25 eV/5 cm the resulting equilibrium shear flow velocity is several times as large as the diamagnetic drift velocity (parameters from Ref. 6). In a nonadiabatic environment this allows the electrostatic potential fluctuations to be larger than the accompanying density fluctuations, since only the former are directly driven by the shear flow. (Strictly speaking, this is only true within the velocity shear layer, however, so other processes must be active in other regions.) Thus, it is relevant to discuss the problem of the usual Kelvin-Helmholtz instability with the additional effect of magnetic shear-induced resistive dissipation but neglecting the effects of density perturbations with all the drift-wave complications the latter involve.

The principal effect of the sheared magnetic field is to provide a new energy sink in addition to the viscous sink. The sole driving source is the sheared flow, which is externally maintained. The model is a sheared slab with a linearly varying sheared component in the magnetic field. The equilibrium flow is along flux surfaces and is

given a hyperbolic tangent profile, so that there is a pronounced vorticity maximum. We assume for simplicity that the magnetic field is aligned so that it is perpendicular to the flow and to the flow gradient at the vorticity maximum. Thus, at the vorticity maximum (where the driving is strongest) the magnetic field has little effect, and is simply convected around. Away from this resonant layer, the flow must cross flux surfaces as it is too weak to bend them. Resistive dissipation is involved, and the less resistive the plasma is, the more effective the magnetic shear is in stabilising the perturbations. This is a form of line-tying. The important difference between the viscous and resistive sinks is that while the former is local, in wavenumber space, the latter is *spatially* local. The effect of the resistive sink comes into play when an initially unstable wavelike perturbation nonlinearly broadens as a result of entrainment by turbulent vorticity diffusion of the surrounding fluid. As the initial eddies grow they form secondary shear flows which further break off smaller eddies from the surroundings and incorporate them into the widening turbulent layer. As this layer thus broadens it samples more and more magnetic shear, *i. e.*, resistive dissipation. If the shear is sufficiently strong this additional dissipation results in premature saturation of the driven turbulence. "Premature", because it takes place before the nonlinear cascade is fully developed. In the strong shear limit, assuming the initial perturbation is linearly unstable, resistive dissipation takes over from viscosity as the dominant saturation mechanism. This was first argued and shown using a statistical closure analysis,[7] about which more will be said in Section III.

Our purpose here is to develop and implement a numerical model to study the physics of nonlinear broadening and the resistive dissipation path to saturation. We also study the transition regimes, one near the linear stability boundary and the other where the resistive dissipation mechanism loses its dominance. These regimes are important in determining the extent of the strong shear regime and require the ability to work where

the assumptions of the theory fail. The principal numerical problem is the incorporation of the magnetic shear (line-bending) term into the scheme. In the boundary regions and at high wavenumber the resistive disspation is much faster than the characteristic shear-flow timescale, so the line-bending term must be handled implicitly. Otherwise, the computations would have to be carried for millions of timesteps, as we will show. On the other hand, an implicit scheme with a large timestep might be inaccurate. We argue in Section IV that it is only necessary to resolve the dissipation process near the resonant layer and for moderate wavenumber, as that is where most of the fluctuation energy actually resides. This is supported by the results of a linear test, in which the numerical scheme reproduces linear growth rates to high accuracy.

Beginning with the next section, we describe in more detail the physical model and derive in the appropriate limits the equation for the $\mathbf{E} \times \mathbf{B}$ vorticity dynamics. Then, in Section III, we discuss the special characteristics of the resistive energy sink alluded to above and expand the discussion on the physics of the saturation mechanisms. Section IV contains the details of the numerics, particularly the implicit treatment of the resistive dissipation term, but also the problems of resolution and scale separation. Sections V and VI contain the results of the computations for weak and strong magnetic shear, respectively. The former regime is that in which the nonlinear cascade is the dominant mechanism for the energy transfer. In the limiting case the physics are those of 2D Kelvin-Helmholtz turbulence without the magnetic field. Strong spatial broadening occurs along with the formation of intermittent structure in the vorticity which bears similarities to that observed by McWilliams in studies of decaying Navier-Stokes turbulence.[8] The strong magnetic shear regime is characterised by nonlinear mode broadening, sufficient to access the resistive dissipation and dynamically enforce marginal stability. The saturated amplitutes in this regime are small, so that the linear driving terms in the convective operator are the largest. Here also, the viscosity is seen

not to play an important role. We find that the fluctuation amplitude scaling with magnetic shear observed from the numerical results agrees closely with that predicted by the statistical closure analysis. The implications of these results are further discussed in Section VII.

II. Model Equation

We begin with an illustration of the physical situation under consideration. This is shown in Fig. 1. The geometry is that of a sheared slab, chosen to model a thin annular region (in minor radius) near the resonant surface of a given helicity in a tokamak edge plasma. The magnetic field is dominantly in the (toroidal) z-direction but has a small, sheared y-component which varies linearly with the radial distance from the resonant surface, x. The resonant surface is located where $k_{||} \equiv \mathbf{k} \cdot \mathbf{B}/|\mathbf{B}|$ vanishes (the disturbances are periodic in y with a fundamental wavenumber of $\mathbf{k}_0 = k_0 \hat{\mathbf{y}}$). Thus, $k_{||} = k_0 x/L_s \equiv k'_{||} x$. There is a sheared radial electric field which gives rise to an $\mathbf{E} \times \mathbf{B}$ velocity profile of the form $\mathbf{v}_E = v_E \hat{\mathbf{y}} = v_0 \tanh(x/\Delta_E)\hat{\mathbf{y}}$. For simplicity this is assumed to be coincident with the magnetic field so that B_y and v_E vanish at the same place ($x = 0$). We will briefly discuss in the last section the result of relaxing this precondition. Nonalignment would effectively mean line-tying, which leads to enhanced dissipation as well as fluctuation asymmetry with respect to the vorticity maximum. To avoid complication from drift-wave effects we will assume that the diamagnetic drift velocity is small compared to v_0 and that the plasma dynamics are strongly hydrodynamic. We may as a result neglect density fluctuations in favor of those in the electrostatic potential, related to velocity fluctuations by $\tilde{\mathbf{v}} = (c/B)\hat{\mathbf{z}} \times \nabla\tilde{\phi}$. An additional condition is that the resistive skin time of the velocity shear layer is short compared to the characteristic flow timescale so that magnetic field fluctuations are

prevented [$\Delta_E^2 k_0 v_0 (4\pi/\eta c^2) \ll 1$]. (As we will show, this is the condition for the electrostatic limit.) Otherwise, the system would be stable, as we are also assuming a weak flow ($v_0/v_A \ll \Delta_E/L_s$).

In Ref. 7 the equation describing the fluctuations in this model was derived from the perspective of reduced MHD.[9] Here, we take a different approach which will make clear the conditions under which we can neglect density fluctuations. This will also illustrate that the problem at hand is a limiting case of drift waves driven by shear in the $\mathbf{E}\times\mathbf{B}$ velocity profile. The characteristic spatial and temporal scales are $x \sim \Delta_E$ and $\partial/\partial t \sim k_0 v_0$. It is instructive, however, to start from drift-wave ordering, and then convert that system of equations to the shear flow problem. The approach we use is to begin with the equations for drift-tearing modes coupled to sound waves, which have been previously derived[10,11]:

$$\frac{1}{c}\frac{d}{dt}\psi = -\eta J_\parallel + \frac{T}{ne}\nabla_\parallel n, \tag{1}$$

$$\frac{d}{dt}\nabla_\perp^2\phi = 4\pi\frac{v_A^2}{c^2}\nabla_\parallel J_\parallel, \tag{2}$$

$$\frac{d}{dt}n = \frac{1}{e}\nabla_\parallel J_\parallel - n\nabla_\parallel u_\parallel, \tag{3}$$

$$\frac{d}{dt}u_\parallel = -\frac{c_s^2}{n}\nabla_\parallel n + \mu_\parallel\nabla_\parallel^2 u_\parallel, \tag{4}$$

where T and n are the electron temperature and density, ψ, $J_\parallel$, and $u_\parallel$ are the parallel magnetic vector potential, current, and ion velocity, $v_A \equiv B/(4\pi n M_i)^{1/2}$ and $c_s \equiv \sqrt{T/M_i}$ are the Alfvén and sound velocities, and d/dt is the convective derivative. For the convective derivative, the stream function for the cross-field velocity is $(c/B)\phi$, in which is included the equilibrium shear flow as well as the fluctuations. Quasineutrality and cold ions are assumed, the latter for tractability.

In the absence of magnetic islands the condition under which we can neglect fluctuations in ψ is the same as that for the constant-$\tilde{\psi}$ assumption for tearing modes:

$\beta L_s^2/L_n^2 \ll 1$. Well satisfied in an edge plasma, this condition assumes drift-wave ordering: $x \sim \Delta_D$ and $(\partial/\partial t) \sim \omega_*$. [Here, $\Delta_D \equiv (\omega_* \nu_e)^{1/2}/k'_\parallel V_e$.] But the condition is even easier to meet ($v_0 > v_D$ but $\Delta_E < \Delta_D$) for the shear-flow scales [$x \sim \Delta_E$ and $(\partial/\partial t) \sim k_0 v_0$]. For the shear-flow case the condition becomes $\Delta_E^2 k_0 v_0 (4\pi/\eta c^2) \ll 1$. Physically this states that the resistive skin time of the velocity shear layer must be short compared to the characteristic flow timescale. For each ordering, these are the conditions under which the electrostatic limit is valid. In this limit the Ohm's law is

$$\eta J_\parallel = \frac{T}{ne} \nabla_\parallel n - \nabla_\parallel \phi. \tag{5}$$

This equation describes the fact that parallel currents are confined to the hydrodynamic layer, outside which $\widetilde{n}/n = e\widetilde{\phi}/T$. Using this in Eqs. (2,3) we arrive at the system of equations for magnetic shear-localised, nonadiabatic drift waves[12]:

$$\frac{d}{dt} \nabla_\perp^2 \phi = -4\pi \frac{v_A^2}{\eta c^2} \left(\nabla_\parallel^2 \phi - \frac{T}{ne} \nabla_\parallel^2 n \right), \tag{6}$$

$$\frac{dn}{dt} = \frac{V_e^2}{\nu_e} \left(\nabla_\parallel^2 n - \frac{ne}{T} \nabla_\parallel^2 \phi \right) - n \nabla_\parallel u_\parallel, \tag{7}$$

together with Eq. (4).

We now proceed to eliminate the density fluctuations from consideration and with them the complicating drift-wave physics. The essential ingredients are the conditions $v_0 > v_D$ and $(\Delta_E, \Delta_S) < \Delta_D$. Given a level of potential fluctuations, the two effects that drive accompanying density fluctuations are density gradient free energy and the parallel diffusion process. The first will yield a density response of the order

$$\widetilde{n}/n \sim (\partial/\partial t)^{-1} (ck/B)(\partial n/\partial x)\widetilde{\phi} \sim (v_D/v_0)(e\widetilde{\phi}/T).$$

On the other hand, if Δ_D is necessarily within the system, *i. e.*, if it is less than either Δ_E or Δ_S, then we will have regions in which the fluctuations are adiabatic. However, if the second condition is satisfied, then the fluctuations will be driven and damped

within the hydrodynamic region, and the density will not have time to react. Under these conditions the system of equations reduces to one[7]:

$$\frac{d}{dt}\nabla_\perp^2\phi = -4\pi\frac{v_A^2}{\eta c^2}\nabla_\parallel^2\phi.$$

To perform the calculations we work in normalised units, in which x, y, and t are scaled by Δ_E, k_0^{-1}, and $(k_0 v_0)^{-1}$. The potential, ϕ, is scaled by $(T\Delta_E/eL_n)(v_0/v_D)$, or equivalently $\Delta_E E_r$, where the radial electric field is evaluated away from the velocity shear layer. As stated above, we work with a model profile in which $v_E \propto E_r \propto \tanh(x/\Delta_E)$. The equation to be solved in these units is

$$\frac{\partial}{\partial t}\nabla_\perp^2\tilde{\phi} = -\tilde{\mathbf{v}}\cdot\nabla\nabla_\perp^2\tilde{\phi} - v(x)\frac{\partial}{\partial y}\nabla_\perp^2\tilde{\phi} + \Omega(x)\frac{\partial}{\partial y}\tilde{\phi} - R\nabla_\parallel^2\tilde{\phi} + D\big(\nabla_\perp^2\tilde{\phi}\big), \qquad (8)$$

where $v(x) = \tanh x$ and $\Omega(x) = -2\tanh x\,\mathrm{sech}^2 x$ are the normalised profiles of the $\mathbf{E}\times\mathbf{B}$ velocity and vorticity derivative, $\nabla_\parallel = x(\partial/\partial y)$, and D is an operator modelling perpendicular dissipation at small scales. The important parameter is R, which defines ratio of the dissipation-free channel width to Δ_E. This width, Δ_S, is determined by a balance between the equilibrium flow drive and the resistive dissipation:

$$\begin{aligned}
\mathbf{v}\cdot\nabla\nabla_\perp^2 &\sim 4\pi\frac{v_A^2}{\eta c^2}\nabla_\parallel^2, \\
k_0 v_0 \Delta_S^{-2} &= 4\pi\frac{v_A^2}{\eta c^2}\frac{k^2}{L_s^2}\Delta_S^2, \\
\frac{\Delta_S^4}{\Delta_E^4} &= \frac{1}{K}\frac{\tau_A^2}{\tau_R\tau_v} \equiv R^{-1},
\end{aligned} \qquad (9)$$

where $\tau_A \equiv L_s^2/v_A^2$, $\tau_R \equiv 4\pi\Delta_E^2/\eta c^2$, and $\tau_v \equiv \Delta_E/v_0$ are the hydromagnetic, resistive, and velocity transit times, respectively, and $K \equiv k_0\Delta_E$. K also appears in $\nabla_\perp^2 \equiv (\partial/\partial x)^2 + K^2(\partial/\partial y)^2$.

The first three terms on the right side of Eq. (8) represent nonlinear convective transfer, linear shear flow convection and driving, and linear resistive dissipation. As is made computationally necessary by the absence of k_x-space dissipation in the magnetic

shear we have added an artificial viscous dissipation term. This is called artificial because we employ a hyperviscosity of the form $D = -\mu_\perp \nabla_\perp^4$ rather than the usual $D \propto \nabla_\perp^2$ to confine the dissipation range of D to the smallest scales. Although it does not correctly model the process of fluid viscosity, the hyperviscosity is adequate for our purposes because we are most interested in the regime in which resistive dissipation is the dominant energy sink. Eq. (8) is essentially the same as Eq. (9) of Ref. 7. Note that our R is their KR^2.

III. The Roles of Broadening and Shear Localisation

To concentrate our attention on the nonlinear interaction physics we assume the equilibrium to be externally maintained, *i. e.*, B_y and v_E are not allowed to evolve in time. The energetics of the system are then as follows. There is a source at long wavelength arising from the maintenance of the shear in the $\mathbf{E} \times \mathbf{B}$ velocity. Energy sinks result from viscous dissipation at small scales and resistive dissipation due to the magnetic shear. While the source is localised to the velocity shear layer, the resistive sink is only effective outside the magnetic shear channel, of width Δ_S. This latter is a consequence of the shear in the magnetic field, *i. e.*, greater displacement from the resonant surface indicates larger $k_\parallel$. Because the field is thus less favorably aligned, the fluctuations are subject to more parallel dissipation. While these are linear effects, energy can be carried from source to sink only by nonlinear processes arising from fluid convection (assuming initial linear instability). Note that the sinks act very differently. For viscous dissipation to act, energy must cascade from large to small scales in the usual way. On the other hand, the existence of a linearly unstable perturbation indicates minimal overlap between the source and resistive sink. Thus, for resistive dissipation to be effective the spatial extent of the velocity fluctuations must be increased, *i. e.*, "mode broadening" must occur.

Mode broadening is a natural consequence of the cascade process through which energy produced at large scales is carried to the smallest scales, where it is removed by viscous dissipation. Consider a linearly unstable eddy which is being driven by the equilibrium flow shear. The flow associated with this eddy also has shear and will drive still smaller eddies at its edges, and so on. This can also be thought of as a process of turbulent self-convection or vorticity diffusion. Broadening occurs as a result of this progressive entrainment of additional fluid at the edges of the larger eddies. When the magnetic shear is sufficiently weak it plays little or no role, and saturation occurs when enough energy is being cascaded to the viscous scales to compensate that which is input by the maintenance of the equilibrium flow.

Strong magnetic shear is, however, another matter. At the resonant surface, aligned for simplicity with the equilibrium vorticity maximum, there is no variation along field lines and consequently there is no parallel dissipation. Away from this surface the magnetic field component aligned with the wavenumber of the mode becomes larger, and so does the importance of the parallel dissipation. Physically, where there is magnetic shear the eddies must resistively slip past the field lines (due to the restriction that they are not capable of bending the field lines) if they are to remain active. Thus, there is an additional energy sink located not in k-space at small scales but in configuration space away from the resonant surface. (Of course the sink is also stronger for higher k_y.) The dissipation-free channel will be of a width, Δ_S, determined by the balance between the equilibrium flow drive and the resistive dissipation illustrated in Eq. (9). As the unstable eddy becomes of finite magnitude it begins to broaden as usual, but if Δ_S is only marginally larger than Δ_E this process stops when the eddy feels the effects of resistive dissipation (if $\Delta_S < \Delta_E$ the eddy will be stable). This energy sink is directly accessed, shutting off the nonlinear cascade process. It is not a linear process which is active, however. While two linear processes are in balance it is

the nonlinear convection which is in fact responsible for the broadening and therefore the energy transfer from source to sink.

The energetics of the system are incorporated in the governing equation, Eq. (8). The total energy is just that in the fluid velocity fluctuations,

$$E \equiv \int_{-\pi}^{\pi} \frac{dy}{2\pi} \int_{-x_L}^{x_L} dx \, \frac{1}{2} \left| \nabla \widetilde{\phi} \right|^2 , \tag{10}$$

where x_L is some boundary within which they are localised. An equation for it can be had by multiplying Eq. (8) by $-\widetilde{\phi}$ and integrating over all space by parts:

$$\begin{aligned} \frac{\partial E}{\partial t} &= \left\langle -\widetilde{\phi} \frac{\partial}{\partial t} \nabla_\perp^2 \widetilde{\phi} \right\rangle \\ &= \left\langle v(x) \widetilde{\phi} \frac{\partial}{\partial y} \nabla_\perp^2 \widetilde{\phi} \right\rangle - \left\langle \Omega(x) \widetilde{\phi} \frac{\partial \widetilde{\phi}}{\partial y} \right\rangle + R \left\langle x^2 \widetilde{\phi} \frac{\partial^2 \widetilde{\phi}}{\partial y^2} \right\rangle - \left\langle \widetilde{\phi} D \nabla_\perp^2 \widetilde{\phi} \right\rangle , \end{aligned}$$

where the angle brackets represent the integrations taken in Eq. (10) and the integration over the $\widetilde{\mathbf{v}} \cdot \nabla$ term vanishes due to incompressibility. Because of the periodicity in y the second term on the right side of this equation also vanishes. The first term is integrated by parts, and also because of the periodicity in y only the velocity gradient piece survives. The third term is also integrated by parts. Lastly, because in general the dissipation operator involves an even number of derivatives it is integrated by parts once for every two of them plus once more for the $\nabla_\perp^2$ in the vorticity. In our case there are four derivatives. The resulting form of the energy equation becomes

$$\frac{\partial E}{\partial t} = - \left\langle \frac{\partial v(x)}{\partial x} \widetilde{v}_x \widetilde{v}_y \right\rangle - R \left\langle (x \widetilde{v}_x)^2 \right\rangle - \mu_\perp \left\langle \left| \nabla \nabla_\perp^2 \widetilde{\phi} \right|^2 \right\rangle , \tag{11}$$

where for illustraton purposes we have written the fluctuating velocities directly: $(\widetilde{v}_x, \widetilde{v}_y) = (-\partial \widetilde{\phi}/\partial y, \partial \widetilde{\phi}/\partial x)$. Whether the first term on the right side of Eq. (11) is a source or sink depends on the access of the free energy in the velocity gradient by the fluctuations. In the energy-producing range the flow cells will be oriented so that $\widetilde{v}_x \widetilde{v}_y$ is negative. (See Fig. 8 for an illustration.) This controls the linear stability boundary

in terms of K in the absence of magnetic shear. The last two terms in Eq. (11) zzz- are the sinks discussed above. Note by the second term that only the x-component of $\tilde{\mathbf{v}}$ contributes to magnetic shear dissipation. This is due to the fact that it is a resistive sink: only the x-component involves motion across flux surfaces. The relative importance of the two sinks is determined entirely by the sizes of R and $\mu_\perp$, *i. e.*, higher Reynolds-number flows will have wider regions in R-space in which mode broadening is the active mechanism of saturation.

We briefly digress here in order to recapitulate the main ideas of Ref. 7. Starting from Eq. (8) a one-point statistical closure treatment is performed on the $\mathbf{v}\cdot\nabla$ nonlinearity to recast it in the form of turbulent diffusion. This is taken to model the associated random convection. The diffusion coefficient is given by $D_t = \sum_l D_l$, where D_l is defined by the operator equation $D_l \approx l^2K^2\left|\tilde{\phi}_l\right|^2[(\partial/\partial t) + ilKv(x) - D_t(d^2/dx^2)]^{-1}$. The dependences of the characteristic lengths, saturated amplitude, and vorticity diffusion on R are then determined by balances between energy sources and sinks. In the linear regime, the inner and outer length scales (Δ_i and Δ_o) are obtained from balances between linear convection and driving, and between inertia and resistive damping, respectively. The latter is the same as the balance leading to Eq. (9). Thus, we have $\Delta_i \approx \Delta_E$ and $\Delta_o \approx R^{-1/4} = \Delta_S$.

Nonlinearly, in the strong magnetic shear regime, the inner length scale is found by balancing the driving source with turbulent diffusion. The outer results from the balance between this same diffusion and the resistive sink. This reflects the mechanism of the nonlinear transfer between source and sink that is mediated by the turbulent diffusion. One then uses the vorticity spectrum equation to get the R-dependence of D_t, and uses this to eliminate D_t in the forms for Δ_i and Δ_o. The result is

$$\Delta_i = R^{-5/16}, \qquad \Delta_o = R^{-3/8}, \qquad \text{and} \qquad D_t = R^{-5/4},$$

where D_t is normalised to $k_0 v_0 \Delta_E^2$. Comparing these to the linear values shows the nonlinear lengths to be broadened.

Finally, the operator equation for D_t is used to get the R-dependence of the saturated amplitude. For this purpose, the time derivative is neglected, leaving a recursive definition for D_t. Assuming strong enough turbulence, the linear driving may be neglected. Also, the lowest mode is expected to dominate. What is left is a relation between the saturated amplitude, $\widetilde{\phi}_{rms}$, the inner length scale, and D_t. This results in an R-dependence of $\widetilde{\phi}_{rms} \approx R^{-15/16}$. The saturated velocity level, v_{rms}, is then obtained by using the inner length scale in the relation $v_{rms} \approx \widetilde{\phi}_{rms}/\Delta_i$, yielding $v_{rms} \propto R^{-5/8}$. It is one of our purposes to check the results of the direct simulation against this scaling.

IV. Numerical Treatment

We now describe how we are to solve Eq. (8). We are interested in a direct numerical simulation for the purpose of performing a check on the existing analytical treatment.[7] The physical system is of finite extent in the x-direction and periodic in y. As the fluctuations are localised, we assume them to vanish at some maximum value of x, which is termed x_L. Typically, $x_L = 20$ is sufficient to provide good behaviour at $x = \pm x_L$. Consistency tests have shown this result as well as the fact that $x_L = 10$ is *not* sufficient. Because of the periodicity in y that direction is handled pseudospectrally, with care taken to avoid aliasing. Using a finite Fourier transform, the number of grid points in the y-direction, N_y, is constrained to be a power of two. To prevent aliasing there are $\frac{1}{3}N_y$ Fourier modes available to the computation.[14] We will refer to the mode number as $l = k_y/k_0$, *i. e.*, $l_{max} = \frac{1}{3}N_y$.

In terms of resolution the tasks are to provide good separation of scales in both directions. Thus, x_L must be large but the inner region $x \sim 1$ must still be well resolved. Similarly, to achieve any separation between the two nonlinear transfer regimes the viscous Reynolds number must be large, *i. e.*, $\mu_\perp \ll 1$. To do this many k_y-modes must be kept for the runs in the $R \ll 1$ regime. This is not so serious a problem for strong magnetic shear, for the resistive dissipation effectively cuts off the spectrum. We keep 85 modes in the former case and 21 in the latter. In the x-direction, $N_x = 256$ points are kept. Because the cascade also operates in k_x this resolution is made necessary by the need to keep $\mu_\perp$ small. The runs are conducted with a hyperviscosity of $\mu_\perp = 10^{-3}$.

Because of numerical stability problems it is impossible to use a fully explicit step with the $\nabla_\parallel^2$ operator. With $R = 0.1$ it is necessary to keep all 85 modes, so the need to resolve the parallel dissipation at the boundary for high-l restricts allowed values of the timestep to

$$\tau \lesssim (R l_{max}^2 x_L^2)^{-1} \sim 10^{-5}. \tag{12}$$

This is clearly too severe, as runs must be carried for up to 100 transit times! Physically, however, it is only necessary to *resolve* the resistive dissipation process for the lowest l's, and only where they exist, *i. e.*, time resolution of this process is not necessary at the boundary where the amplitudes are small: it is enough to have resolution in the magnetic shear-free region and strong damping at the boundary. A value which will satisfy this as well as resolving nonlinear transfer in the weak magnetic shear regime is $\tau = 10^{-3}$ (see the test below). Fortunately, this is also computationally feasible. The problem is then to invert the $\nabla_\parallel^2$ term fully implicitly. This is the real reason that the x-direction is finite-differenced, for only in xk_y-space does $\nabla_\parallel$ not involve differentiation. The inversion that is performed is then

$$\phi^{n+1} = (\nabla_\perp^2 - \nabla_\parallel^2)^{-1}(\nabla_\perp^2 \phi)^n, \tag{13}$$

for the n-th timestep, after $(\nabla_\perp^2\phi)^n$ has been updated with a predictor-corrector on the convection operator (including the linear driving terms). The viscous operator is then inverted implicitly in the usual way.

The numerics were tested in the time domain by comparing computed linear growth rates with those obtained from the shooting code used in Ref. 7. For this test only one mode is kept. The initial state is a simple spatial gaussian for $\widetilde{\phi}$. The linear computations are carried until the growth rate has stabilised in time. To obtain a linear growth rate, γ_L, the mode energy, E [defined in Eq. (10)], is calculated every few timesteps. As the separable time dependence of the fluctuation amplitude is assumed to be $\exp(\gamma_L t)$, this growth rate is calculated using

$$\gamma_L = \tfrac{1}{2} E^{-1} \frac{\partial E}{\partial t}. \tag{14}$$

The results of the comparison as a function of R are shown in Fig. 2, in which one can see that our argument concerning a limited need for time resolution is correct: it is important to resolve the parallel diffusion process only where most of the mode energy actually resides.

The typical linear mode structure appears in Fig. 3, which shows the result of a linear run with $R = 0.7$ and $K = 0.03$. The real part retains its symmetry while an imaginary piece of odd symmetry has developed. This represents a vortical perturbation which has become deformed and tilted in the sense that $\langle \widetilde{v}_x \widetilde{v}_y \rangle < 0$. The mode width is defined for the l-th mode as

$$\Delta_l^2 = \int_{-x_L}^{x_L} dx\, x^2 \left|\widetilde{\phi}_l(x)\right|^2 \Big/ \int_{-x_L}^{x_L} dx \left|\widetilde{\phi}_l(x)\right|^2. \tag{15}$$

Hereafter we use this only for the lowest (linear) mode, $l = 1$. The linear mode width for this case is $\Delta_1 = 0.816$, and generally increases with decreasing R, as resistive shear dissipation becomes less effective. This trend is also shown in Fig. 3, in the form of a plot of Δ_1 as a function of R.

V. Results – weak magnetic shear

The initial state used for nonlinear computations is an isotropic, random-phase turbulent bath over which is laid a spatial Gaussian envelope:

$$\widetilde{\phi}_{t=0} = e^{-x^2/2\delta^2} \int d^2k\, A_k^{1/2} e^{i\mathbf{k}\cdot\mathbf{x}} e^{i\theta}, \tag{16}$$

where $\delta = 2.0$ is the localisation width, $\mathbf{k}$ is a dummy wavenumber, $A_k \propto k/\left[1+(k\rho_s)^4\right]$ is the amplitude spectrum, and θ is a random variable with a flat distribution in the interval $(-\pi, \pi)$. This initial state, displayed in Fig. 4, is normalised such that the rms integrated velocity is $v_{rms} \equiv (2E)^{1/2} = 1.0$, the "nonlinear threshold" at which $\mathbf{v}\cdot\nabla$ is of order unity.

A series of nonlinear computations was performed, spanning the range in R from the linear stability boundary (slightly greater than unity) to well within the turbulent cascade regime. The values of R used were 1.0, 0.7, 0.5, 0.3, 0.2, 0.1, and 0.01. The first four carried 21 Fourier modes; the fifth, 42; and the last two, 85. For all cases the other parameters took the values $K = 0.03$ and $\mu_\perp = 10^{-3}$. They were run from $t = 0$ to $t = 100$, except for the last which saturated earlier by $t = 60$.

The $R = 0.01$ case is firmly within the cascade regime and is fully described herein as an example of that regime. As one can see from Fig. 5, the flow energy spectrum is very broad and peaked near the most unstable modes. The exact mode number of the spectrum peak fluctuates up and down about the mean by a few modes, but the mean is stationary in time. Most of the flow energy is within a few modes of the maximum. The sharp drop near $\frac{2}{3}l_{max}$ indicates adequate resolution, *i. e.*, the hyperviscosity is sufficient to truncate the cascade without washing out the energy-containing region of the spectrum. The interval in time at which spectra are computed is $\delta t = 1.0$, far too long to estimate the eddy turnover time, τ_E, by measuring energy transfer rates directly from changes in the spectrum itself. The strong time dependence

can be seen in Fig. 6, which displays the time evolution of the energy and $l = 1$ mode width, E and Δ_1. These are again sampled only every $\delta t = 1.0$, and now from the $E(t)$ curve we can see unambiguously the fact that this sampling is too sparse for direct measurment of nonlinear transfer rates. The issue of these rates is addressed in the next section. That the state is saturated, however, is clear.

The presence of nonlinear mode broadening as a result of the cascade process is shown in Fig. 7, which may be taken in contrast with Fig. 3(a). The mode shown here is the fundamental, $l = 1$. It is no longer centered, and is strongly deformed relative to its linear shape. This nonlinear shape changes radically on a time scale of order τ_E, and the strength of the turbulence may also be seen from the fluctuations in Δ_1 shown in Fig. 6. As discussed in Section II, this broadening is a natural consequence of the cascade process and is more effective as the amplitude of the fluctuations increases and fluid near the region of the vorticity maximum is more easily entrained.

One other phenomenon which is clearly observed in this regime is the formation of intermittent structure in the vorticity. This is characterised by the dominance of tightly localised vortices in that field. The form of the potential and the vorticity is contrasted in Fig. 8. Only in the vorticity is this intermittence observed. It can be measured by the kurtosis of the fluctuations, defined by $\mathrm{Ku}(\widetilde{\phi}) \equiv \left\langle \widetilde{\phi}^4 \right\rangle \Big/ \left\langle \widetilde{\phi}^2 \right\rangle^2$, where the brackets denote an ensemble average, here represented by integration over the region within a window 20 units wide in x, centered upon $x = 0$. The initial random-phase distribution is used as a benchmark, as the localisation in x will tend to give larger signals than a fully randomised distribution which has a kurtosis of 3. This benchmark is about 10, so the difference between $\mathrm{Ku}(\widetilde{\phi}) \sim 10$ and $\mathrm{Ku}(\nabla_\perp^2 \widetilde{\phi}) \sim 30$ illustrates the difference in structure of the two fields. Indeed, the noisiness of the run with $K = 0.03$ prevents an even higher signal. An additional run with $K = 0.1$, *i. e.*,

greater separation between the inner layer and dissipation scales, while displaying the same properties as the $K = 0.03$ case yielded an average vorticity kurtosis of over 100.

It is interesting that the overall form of the vorticity structure is similar to that described by McWilliams in simulations of decaying 2D Navier-Stokes turbulence.[8] As shown in Fig. 9 the vortices are nearly circular and represent minima in the turbulent strain field, surrounded by maxima. The turbulent strain is defined as $s^2 = s_1^2 + s_2^2$, where $s_1 = -2\partial^2\widetilde{\phi}/\partial x\partial y$ and $s_2 = \partial^2\widetilde{\phi}/\partial x^2 - \partial^2\widetilde{\phi}/\partial y^2$. The quantity actually plotted is the turbulent "Q", defined as $Q \equiv s^2 - \left(\nabla_\perp^2\widetilde{\phi}\right)^2$. The motivation is to show graphically the alignment of a vortex with a minimum in the positive-definite strain field. The alignment corresponds well with the properties of the vortices of Ref. 8. In both cases, the characteristic lifetime of the structures is far longer than the nonlinear transfer timescale, a property determined in this work by following a given vortex over several $\delta t = 1.0$ snapshot times and noting the rapid transfer timescale from Fig. 6. There are two principal differences in the vortex structure between the two cases. The size of a given structure is random in the isotropic turbulence but tends to be selected here at a value approximately equal to the velocity shear layer thickness. Also, the maxima are ring-shaped in the former case and quadripolar here. These points serve to underscore the fact that the boundary conditions of the shear flow that are important to the vorticity structure in this work are absent in the isotropic case.

Most interesting and important is the relatively uniform size of the vortex structures. Note that we are keeping the equilibrium flow fixed, so that the turbulent shear layer is also of fixed width. This is in keeping with the results of a previous treatment of the turbulent shear layer dynamics by the vortex-in-cell method.[15] In the computations of that work the equilibrium flow was allowed to evolve, starting as a tangential discontinuity and decaying to a widening shear layer with time. Strongly intermittent vorticity was observed, again with nearly circular vortices. The average

size of the vortices was seen to increase with the flow width, although there was no simple scaling relation between the two. At any given time, however, the vortices were all of nearly equal size, as is the case in our results.

Further investigation is necessary to ascertain the implications of the vortices for the cascade process, which is clearly the same for both the turbulent shear layer and isotropic turbulence. However, it is interesting to find these structures in a system which is both driven and damped. Dipole vortices, on the other hand, are never observed to form spontaneously.

VI. Results – strong magnetic shear

The situation is very different when $R > 0.1$, in which case the magnetic shear channel is not much wider than the velocity shear layer. A glance at the spectrum (Fig. 10) is enough to corroborate the argument that the effective process is nonlinear broadening of an essentially linear mode. That is, all or nearly all of the energy lies in the fundamental. This is to be expected from the fact that the saturation amplitude is below nonlinear threshold ($v_{rms} < 1.0$). The case shown ($R = 0.7$, $K = 0.03$) has a saturated v_{rms} of 0.117. The steepness of the spectrum indicates that the cascade process is very ineffective in this regime, leaving nonlinear broadening as the important energy sink.

Fig. 11, showing the mode structure, reveals the tighter localisation in the presence of the strong magnetic shear. Saturation occurs earlier in this environment; when the nonlinear processes cause the mode to broaden, it immediately ceases to grow, shutting off further nonlinear development. The active process, of course, is the dominance of resistive dissipation, which becomes important before a fully-developed nonlinear cascade can be set up. The mode structure is very slightly broadened (to

an average of $\Delta_1 = 0.846$, from the linear value of 0.816). However, since the linear growth rate is weak (see Fig. 2), very little broadening is needed to access the resistive sink.

We can understand this by considering the equation for enstrophy evolution. Multiplying Eq. (8) by the vorticity and integrating over all space we have

$$\frac{\partial}{\partial t}\frac{\left\langle(\nabla_\perp^2\widetilde{\phi})^2\right\rangle}{2} = -\left\langle v_E(x)\nabla_\perp^2\widetilde{\phi}\frac{\partial}{\partial y}\nabla_\perp^2\widetilde{\phi}\right\rangle + \left\langle \Omega_E(x)\nabla_\perp^2\widetilde{\phi}\frac{\partial\widetilde{\phi}}{\partial y}\right\rangle$$
$$- R\left\langle x^2\nabla_\perp^2\widetilde{\phi}\frac{\partial^2\widetilde{\phi}}{\partial y^2}\right\rangle + \left\langle \nabla_\perp^2\widetilde{\phi}D(\nabla_\perp^2\widetilde{\phi})\right\rangle, \tag{17}$$

where the angle brackets represent the integration [as in Eq. (10)]. The first term on the right side vanishes due to the average over y, leaving us with the source and sink terms. Assuming that we are working well within the strong magnetic shear regime we may neglect the term involving D. Modelling the time operator by γ_{NL}, where the subscript NL reflects the full nonlinear value, we have

$$\gamma_{NL} = s_v(\Delta_1) - s_R(\Delta_1), \tag{18}$$

where the source and sink terms are defined by

$$s_v \equiv 2\left\langle(\nabla_\perp^2\widetilde{\phi})^2\right\rangle^{-1}\left\langle \Omega_E(x)\nabla_\perp^2\widetilde{\phi}\frac{\partial\widetilde{\phi}}{\partial y}\right\rangle,$$
$$s_R \equiv 2R\left\langle(\nabla_\perp^2\widetilde{\phi})^2\right\rangle^{-1}\left\langle x^2\nabla_\perp^2\widetilde{\phi}\frac{\partial^2\widetilde{\phi}}{\partial y^2}\right\rangle,$$

and are assumed to be positive definite for small K. These terms are dependent on the mode structure as well as the width, but we are assuming the thrust of the argument of Section III: that the dominant nonlinear effect is the small increase in width of a perturbation which retains its linear structure. If in Eq. (18) the mode width takes its linear value, Δ_1^L, then the left side is the linear growth rate, γ_L. Assuming the mode

width broadens nonlinearly so that

$$\Delta_1 = \Delta_1^L + \delta\Delta, \qquad (\delta\Delta \ll \Delta_1^L)$$

just enough to yield marginal stability, *i. e.*, saturation, Eq. (18) takes the form

$$\gamma_{NL} = s_v(\Delta_1^L) - s_R(\Delta_1^L) + \delta\Delta \frac{\partial}{\partial \Delta_1^L}(s_v - s_R) = 0,$$

where the derivative is evaluated at $\Delta_1 = \Delta_1^L$. We are assuming the R-dependence of γ_L and $\delta\Delta$ to overshadow that of the other quantities in Eq. (17). This will hold best near the linear stability boundary (lowest saturated amplitudes), where small proportional changes in the mode width and shape yield large ones in γ_L and $\delta\Delta$. Of the terms being differentiated s_R has the stronger dependence on Δ_1, so the last term on the right side is negative. The first two terms on the right side give the linear growth rate, so we have

$$\gamma_L = \delta\Delta \frac{\partial}{\partial \Delta_1^L}(s_R - s_v), \qquad \text{or} \quad \delta\Delta \propto \gamma_L.$$

Hence, the change in the mode width of the fundamental should be proportional to the *linear* growth rate. Plotted in Fig. 12 is the observed change in mode width as a function of the linear growth rate. The error bars arise from uncertainties due to the temporal fluctuation of the mode width in the saturated state. These are smaller for weaker turbulence, *i. e.*, smallest saturated amplitudes, as well as for longer runs (larger data set). As expected, the changes in the mode widths increase with decreasing R, ending with a break near $R = 0.1$, where the clean mode structure of Fig. 11 loses its symmetry and centering. Also, the linear relation between $\delta\Delta$ and γ_L is most pronounced for $R > 0.3$, on the side closer to the linear stability boundary, where the assumptions of the previous argument are the most valid. Note that the uncertainties in the broadened Δ_1 become as large as $\delta\Delta$ near the break.

The importance of the mode broadening mechanism in the transition range in R can be seen in the time evolution of E and Δ_1 for $R = 0.3$, shown in Fig. 13. A relaxation oscillation of sorts is occurring, in which the fluctuating mode width drives the total energy up or down, depending on whether the mode width is below or above its saturated average value, respectively. The close correspondence between the two curves demonstrates that the mode broadening process is still dominant in controlling the evolution of the velocity fluctuations.

The break in regimes is also reflected in the scalings of the saturated amplitude, defined by $v_{rms} \equiv (2E)^{1/2}$. This quantity is plotted in Fig. 14, in the form of a dot for each value of R used. The error bars are estimated in the same way as for Fig. 12. The R-dependence given by the renormalised theory,[7]

$$v_{rms} \propto R^{-5/8},$$

is plotted as a dashed line. This line has been amplitude-fit to the four points $R = (0.2 \ldots 0.7)$ by the least squares method. While the point $R = 1.0$ is within the mode-broadening regime, it is too close to the linear stability boundary to agree with the theoretical scaling. This scaling assumes strong turbulence in the sense that the turbulent diffusion dominates linear driving in the saturated state near the vorticity maximum. Approaching the linear stability boundary this assumption fails, as the fluctuation amplitude becomes vanishingly small. The linear relation between the broadening and the linear growth rate, on the other hand, assumes the mode is close enough to linear stability that the fastest R-dependences lie in those quantities. Thus, there is no difficulty with the $R = 1.0$ point in Fig. 12. At the other end, the break to the cascade regime occurs for $R \approx 0.1$, and the scalings no longer apply. Within these limits, the analytical scaling of Ref. 7 is seen to be consistent with the computational results.

VII. Discussion

The computations described in this paper have supported the saturation mechanism for Kelvin-Helmholtz instabilities in a sheared magnetic field that was proposed in Ref. 7. When the resistive shear dissipation width given in Eq. 9 is sufficiently narrow that the sink region begins to overlap the velocity shear layer a new regime is encoutered. Here, the usual nonlinear transfer mechanism by eddy cascading is no longer dominant. The turbulent entrainment of outside fluid by broadening the region of potential fluctuations causes the direct access of the resistive energy sink and saturates the instability before a cascade is set up. This is a relatively narrow regime: the transition occurs near $R = 0.1$ in the case of a hyperviscosity of $\mu_\perp = 10^{-3}$. Presumably, a higher Reynolds number would lead to a wider broadening regime, since the resistive sink would then have greater relative importance than the viscous. We have not been able to test this, being limited in terms of computational resources. As expected, the broadening becomes more pronounced as R is lowered within the broadening regime, since stronger linear growth must be balanced.

Also of interest is the case in which the resonant surface at $k_\parallel = 0$ is not coincident with the vorticity maximum. That is, there is enhanced overlap between the driving source and the resistive sink to begin with. The mode will tend to reside somewhere between the two locations. It will also exhibit pronounced asymmetry. The result might be very similar to a rippling mode in the presence of a strong shear flow, for which the sink to be balanced by the driving is magnetic shear-induced thermal diffusivity.[16] The physical effect of increasing the overlap will be the same as raising R; the transition between the cascading and broadening regimes will be at lower R, as will the linear stability boundary. In a real system with magnetic shear, however, the dominant mode is the one whose helicity aligns closest with the magnetic field at

the vorticity maximum. This mode experiences the least resistive dissipation and is the most dangerous to confinement, so we have concentrated on the case of perfect alignment to study the physics. Even though in a real system the different helicities tend to couple nonlinearly, the small saturated amplitudes will tend to diminish this effect and the mode resonant at the vorticity maximum will dominate.

Acknowledgments

The authors would like to thank Dr. T. Chiueh for many helpful discussions concerning the theory in Ref. 7, and Dr. J.-N. LeBoeuf for constructive criticism of the numerics. We also recognise the support of the U. S. Department of Energy under Contract No. DEFG0580ET53088.

References

[1]S. Chandrasekhar, *Hydrodynamic and Hydromagnetic Stability* (Dover, New York 1981).

[2]R. E. Slusher and C. M. Surko, *Phys. Rev. Lett.* **40**, 400 (1978); *Phys. Fluids* **23**,2425 (1980).

[3]C. M. Surko and R. E. Slusher, *Science* **221**, 817 (1983).

[4]P. C. Liewer, *Nucl. Fusion* **25**, 543 (1985).

[5]C. P. Ritz, private communication.

[6]C. P. Ritz, R. D. Bengston, S. J. Levinson, and E. J. Powers, *Phys. Fluids* **27**, 2956 (1894).

[7]T. Chiueh, P. W. Terry, P. H. Diamond, and J. E. Sedlak, *Phys. Fluids* **29**, 231 (1986).

[8]J. C. McWilliams, *J. Fluid Mech.* **146**, 21 (1984).

[9]H. R. Strauss, *Phys. Fluids* **20**, 1534 (1977).

[10]D. Biskamp, *Nucl. Fusion* **19**, 777 (1979).

[11]Bruce D. Scott, A. B. Hassam, and J. F. Drake, *Phys. Fluids* **28**, 275 (1985).

[12]Bruce D. Scott, P. W. Terry, and P. H. Diamond, in *Turbulence and Transport*, D. Grésillon and M. A. DuBois, eds. (Editions de Physique, Les Ulis Cedex 1986).; Bruce D. Scott, "A High-resolution Implicit Simulation of Nonlinear Drift-wave Turbulence in a Sheared Magnetic Field", submitted to *J. Comp. Phys.*

[13]C. C. Lin, *The Theory of Hydrodynamic Stability* (Cambridge University Press, Cambridge, 1955).

[14]David Gottlieb and Steven A. Orszag, *Numerical Analysis of Spectral Methods: Theory and Applications*, CBMS-NSF Regional Conference Series in Applied Mathematics, Vol. 26 (SIAM, Philadelphia 1977).

[15]H. Aref and E. D. Siggia, *J. Fluid Mech.* **100**, 705 (1980).

[16]G. S. Lee, L. Garcia, B. A. Carreras, and P. H. Diamond, *Proceedings of the Workshop on Turbulence in Confined Plasmas*, Fusion Research Center, Austin, Texas (1987).

Figure Captions

Fig. 1. The model equilibrium. This is a sheared slab with the $\mathbf{E}\times\mathbf{B}$ velocity inflection point aligned with the $k_{\|} = 0$ resonant surface. The coordinate system of unit vectors is shown.

Fig. 2. Comparison between linear growth rates obtained from this work (dots) and the shooting code of Ref. 7 (lines).

Fig. 3. Linear mode structure for the case $R = 0.7$ and $K = 0.03$, in which the linear mode width $\Delta_1 = 0.816$. Also shown is the linear mode width as a function of R.

Fig. 4. The initial fluctuation distribution described by Eq. (16). Solid (dashed) contours are positive (negative) values. The interval is 0.205 and is linear. Also shown is the initial energy spectrum. l is the mode number.

Fig. 5. Broad spectrum for weak magnetic shear, $R = 0.01$, $K = 0.03$. This has been time-averaged over 30 snapshots during the saturated state ($t = 30$ to 60).

Fig. 6. Time evolution of the total energy, E, and the mode width, Δ_1, for $R = 0.01$. Note the rapid changes, indicative of the nonlinear transfer rate.

Fig. 7. Nonlinear mode structure for the run of the previous figure, taken at $t = 50$. Note the loss of regular shape and centering. Linear mode width was 2.24; this has been broadened to an average of 2.64.

Fig. 8. Contours of potential, $\widetilde{\phi}$, and vorticity, $\nabla_\perp^2\widetilde{\phi}$, for the run and time of the previous figure. The intervals are 0.348 and 0.513, respectively. Note the intermittent structure in the vorticity. The vortex at $(x, y) = (0.2, 3.1)$ is shown enlarged in the inset.

Fig. 9. Structure of the vortices of the previous figure. The vortex at $(x, y) = (0.2, 3.1)$ is seen to be circular. It is located at a minimum in the turbulent strain and is surrounded by maxima, a fact indicated by the contours of the turbulent Q, defined in the text (see inset). The contour interval is 2.18.

Fig. 10. Steep spectrum for strong magnetic shear, $R = 0.7$, $K = 0.03$. This is not time-averaged, but taken at $t = 90$.

Fig. 11. Nonlinear mode structure for the run and time of the previous figure. The structure is very similar to the linear mode but is slightly broadened ($\Delta_1 = 0.846$, compare with 0.816 in Fig. 3).

Fig. 12. Change in mode width, normalised to linear growth rate, as a function of γ_L. Error bars are due to temporal fluctuations, which become large in the transition to the weak magnetic shear regime near $\gamma_L = 0.25$ ($R = 0.2$).

Fig. 13. Time evolution of the total energy, E, and the mode width, Δ_1, for $R = 0.2$. Note the relaxation oscillation operating between them. The mode broadening mechanism is still controlling the saturation.

Fig. 14. Saturated amplitude, v_{rms}, as a function of R. The dashed line, amplitude-fit as stated in the text, shows the scaling from the analytic theory of Ref. 7.

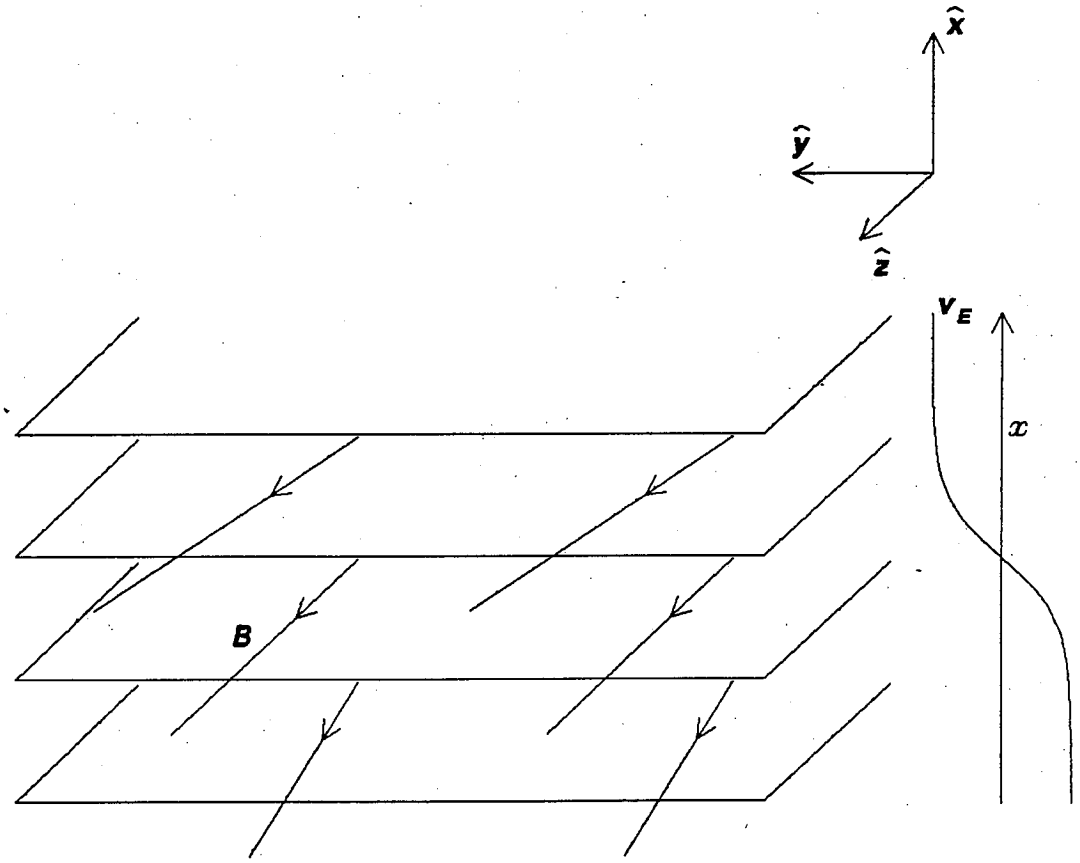

Fig. 1.

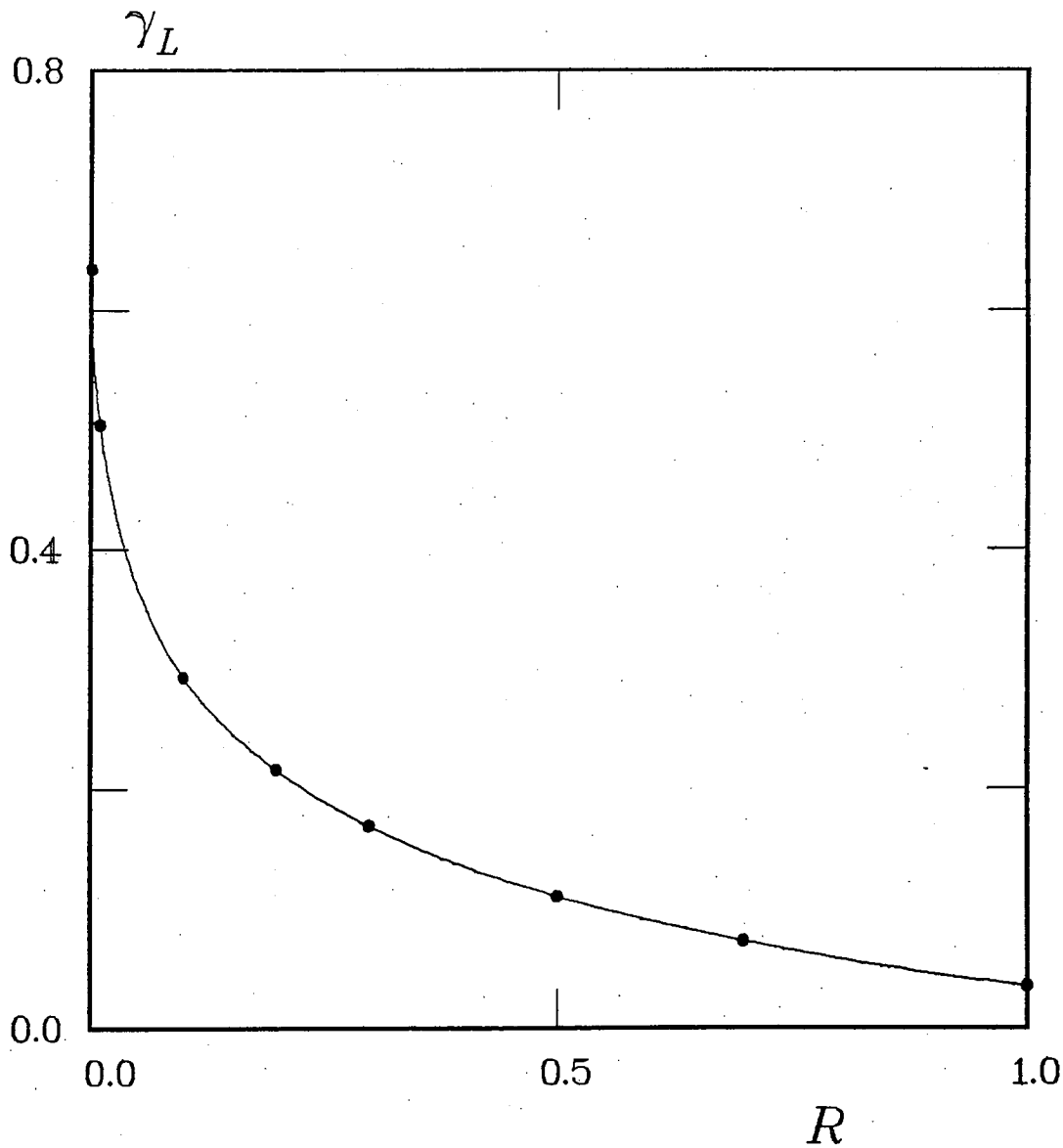

Fig. 2.

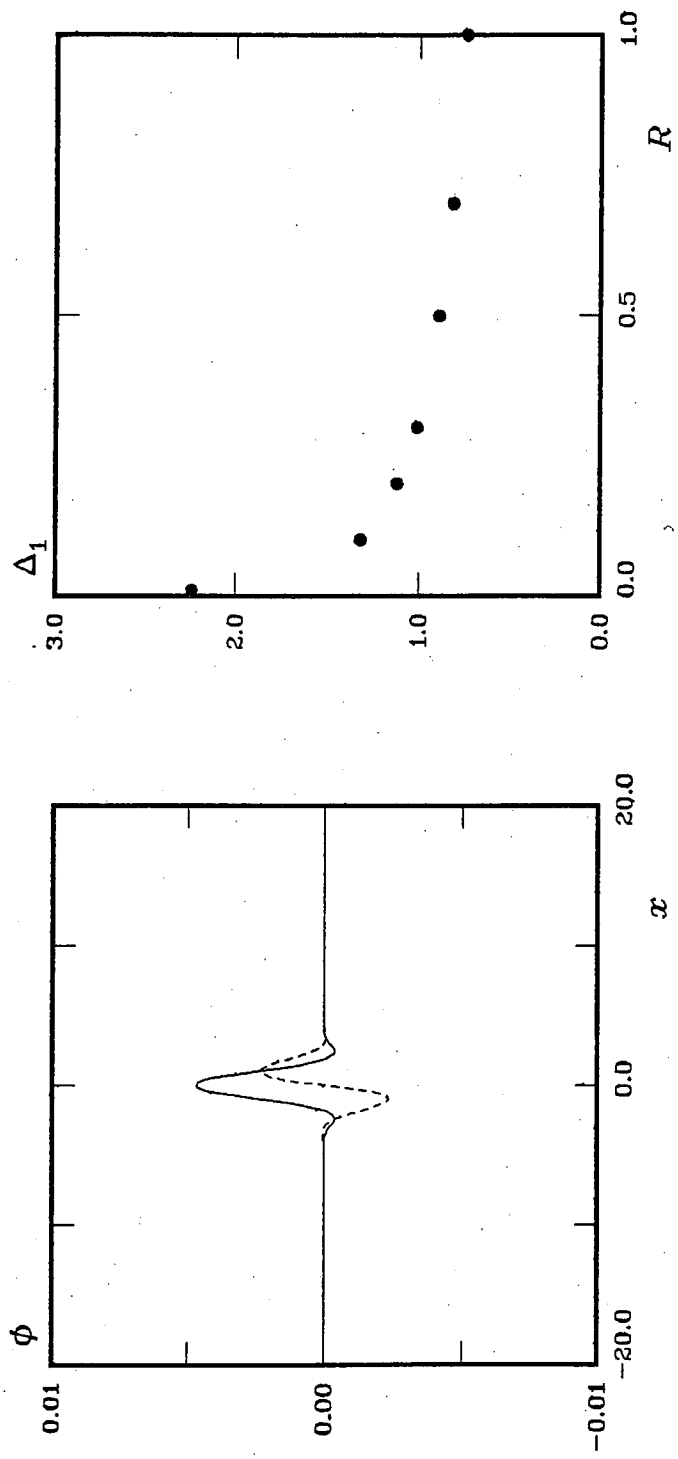

Fig. 3.

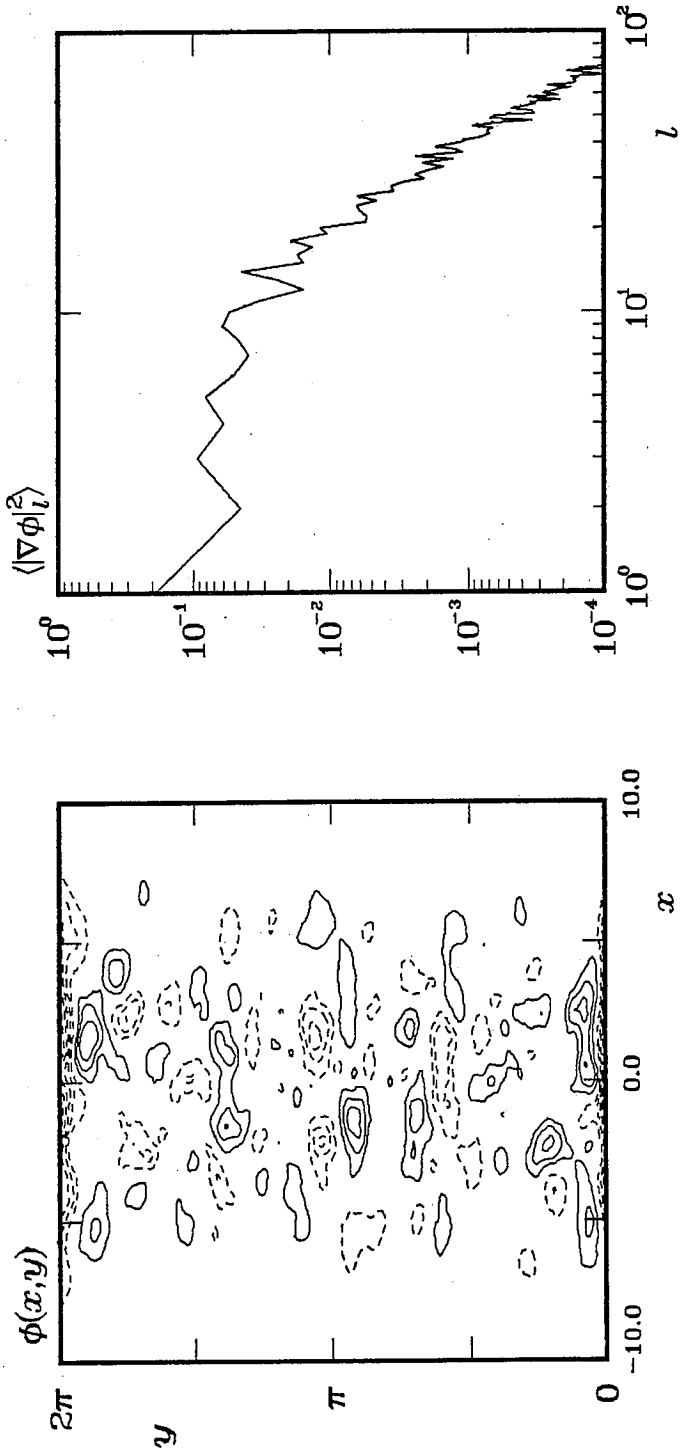
$\phi(x,y)$
2π
π
0
y
10.0
0.0
−10.0
x
$\langle|\nabla\phi|_l^2\rangle$
10^0
10^{-1}
10^{-2}
10^{-3}
10^{-4}
10^0
10^1
10^2
l

Fig. 4.

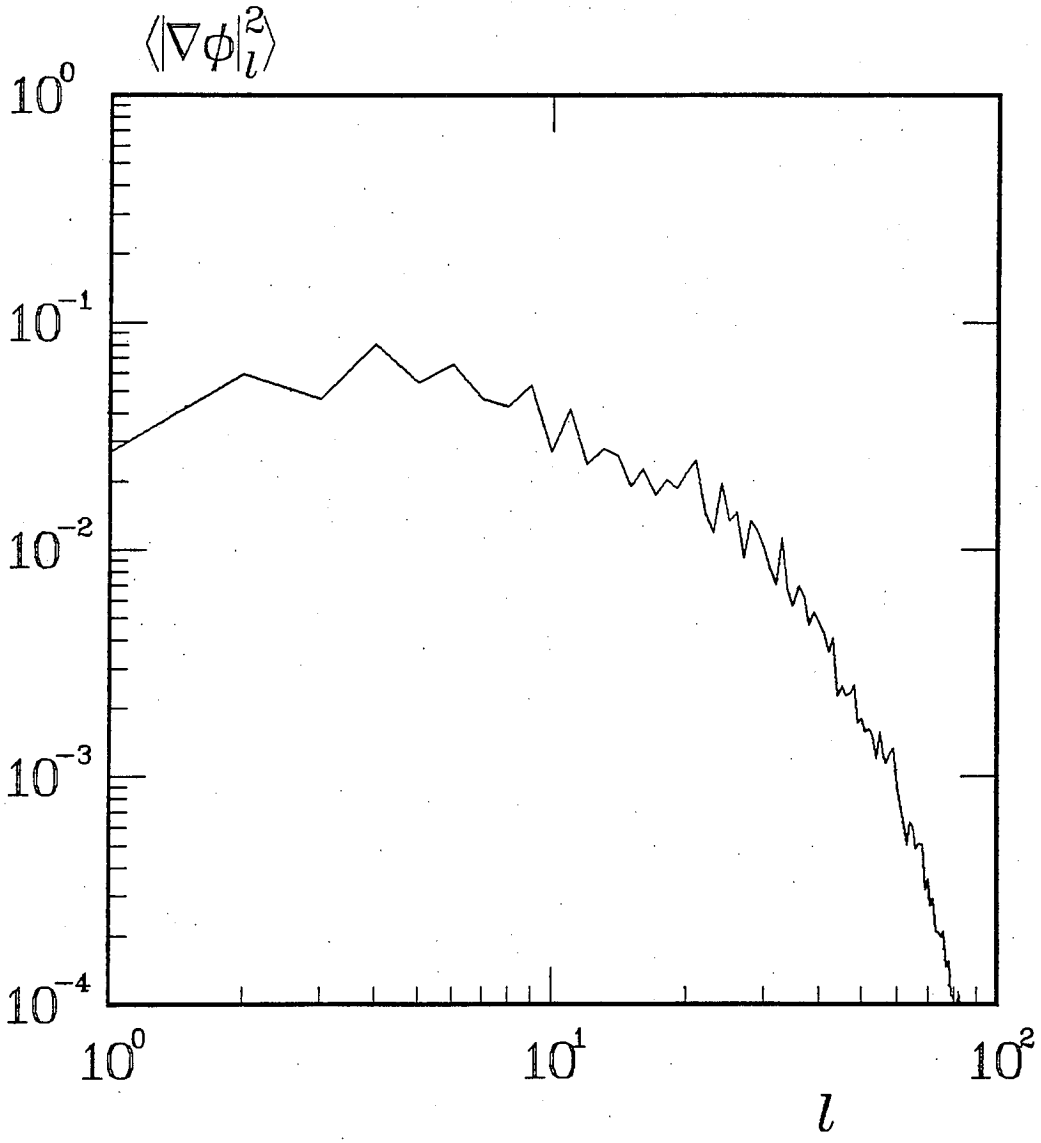

Fig. 5.

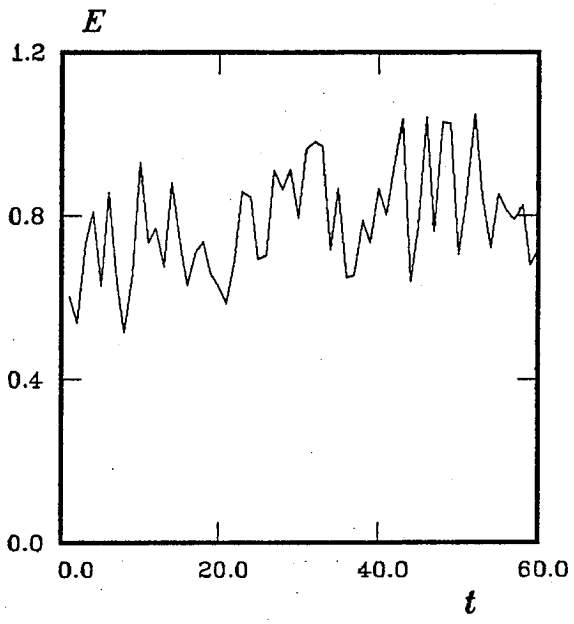

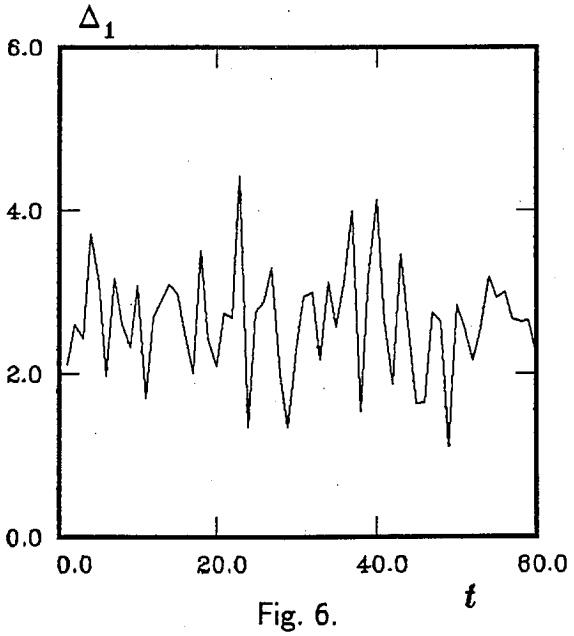

Fig. 6.

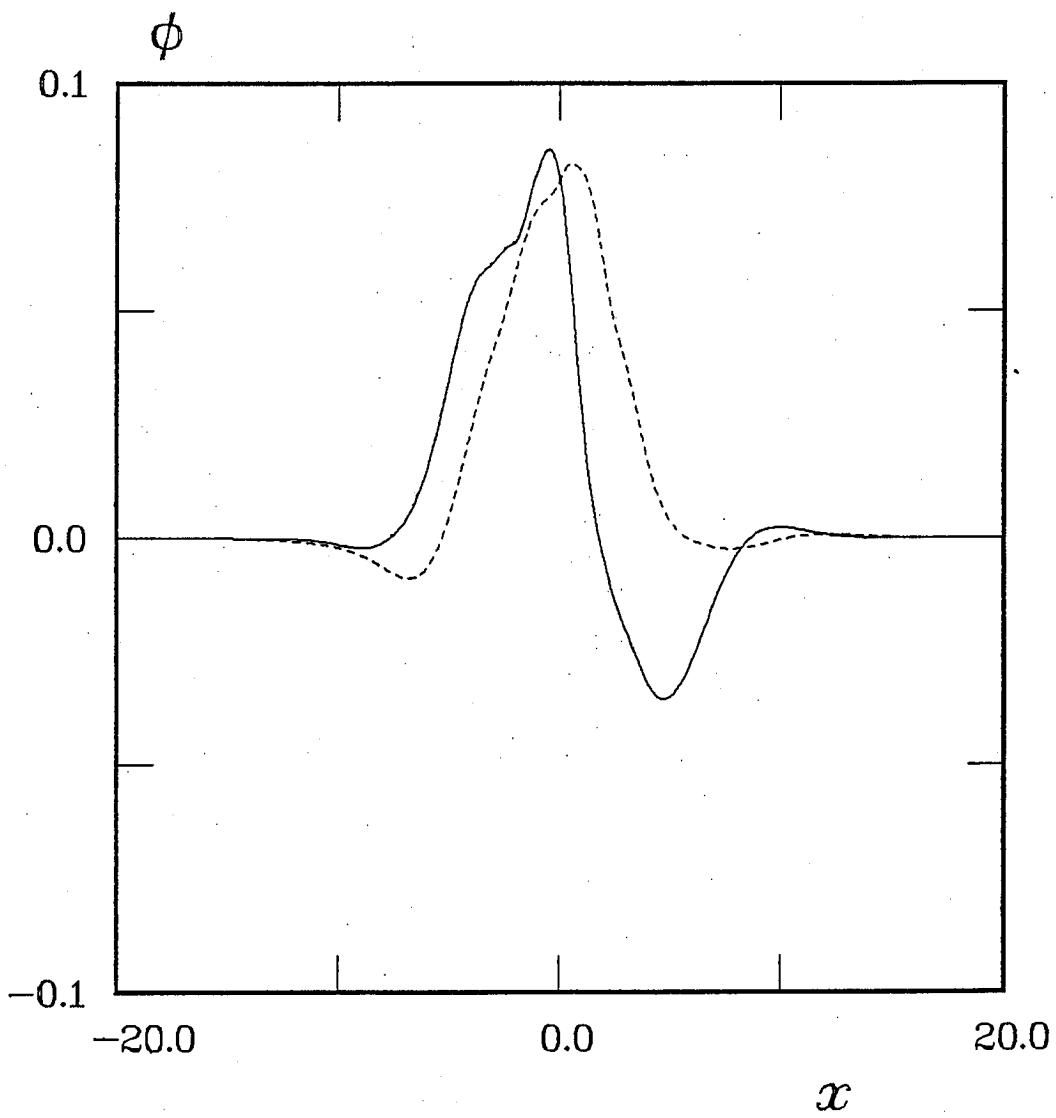

Fig. 7.

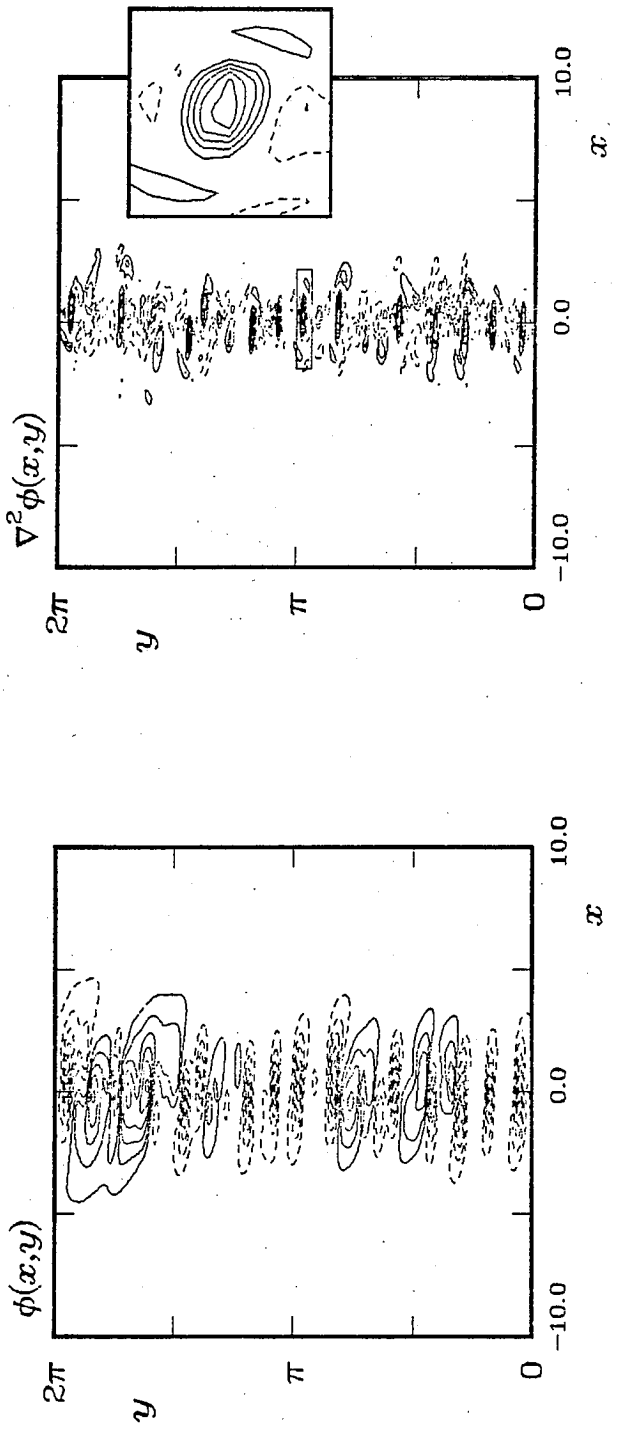

Fig. 8.

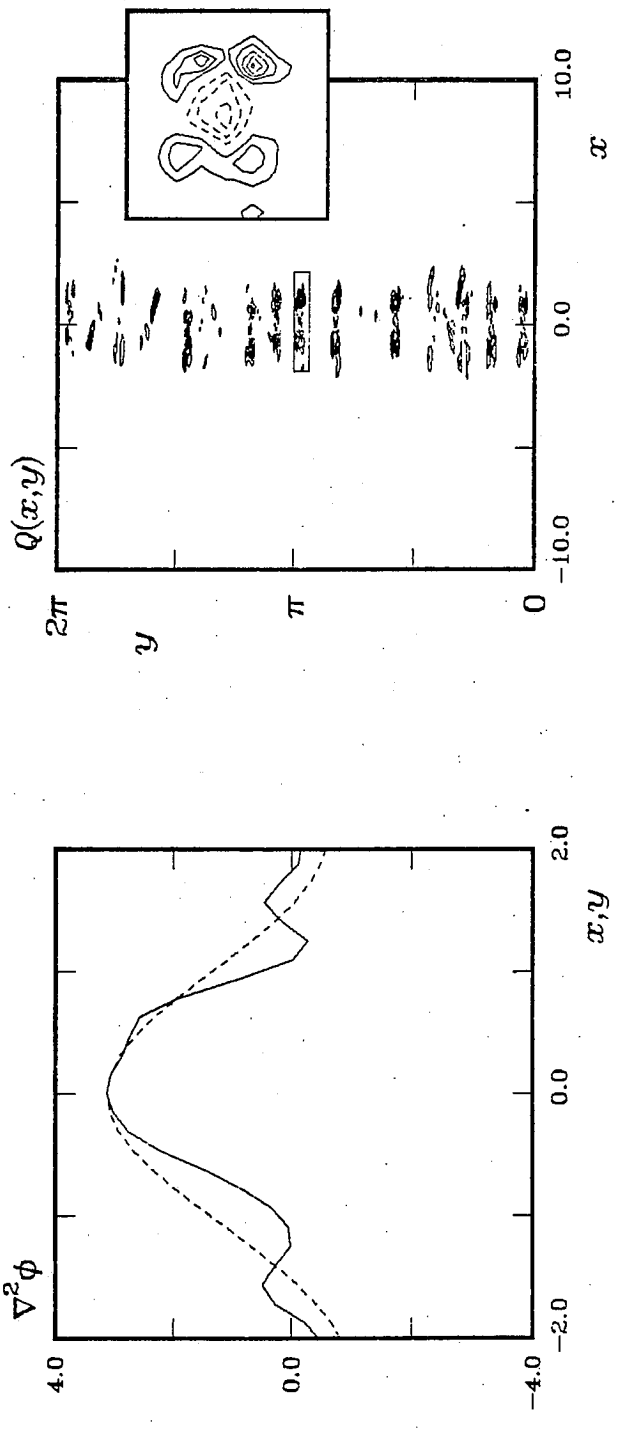

Fig. 9.

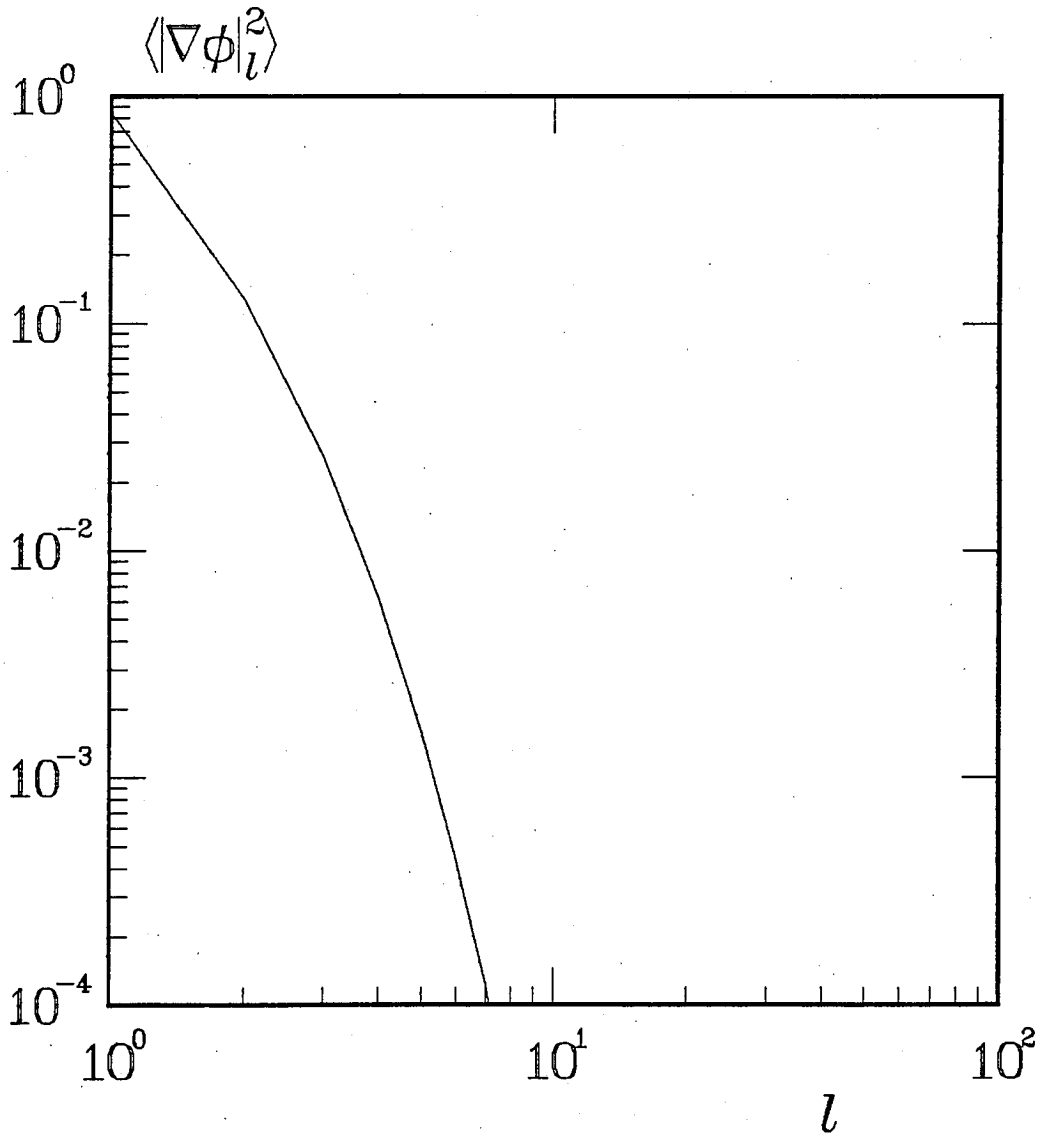

Fig. 10.

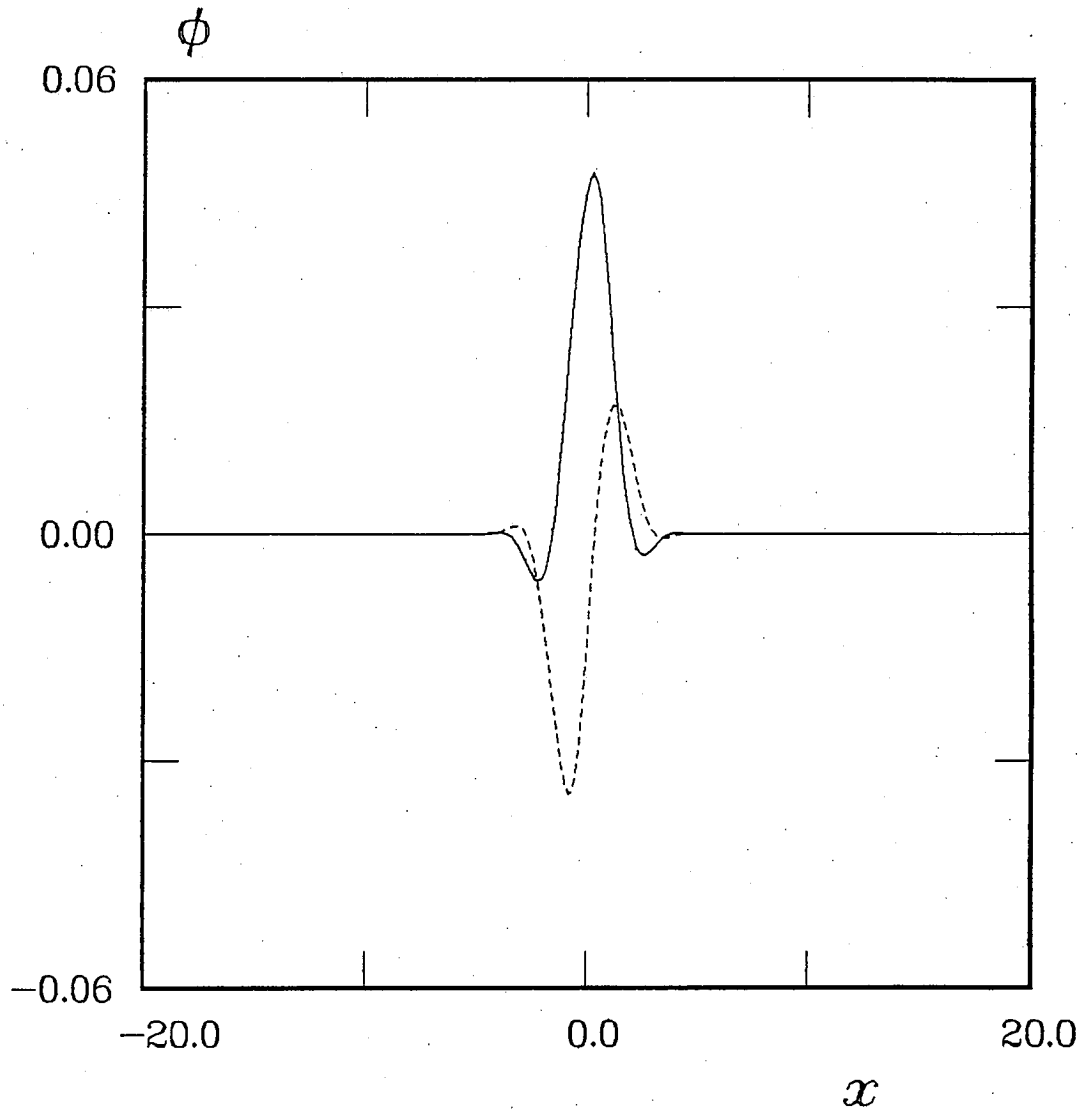

Fig. 11.

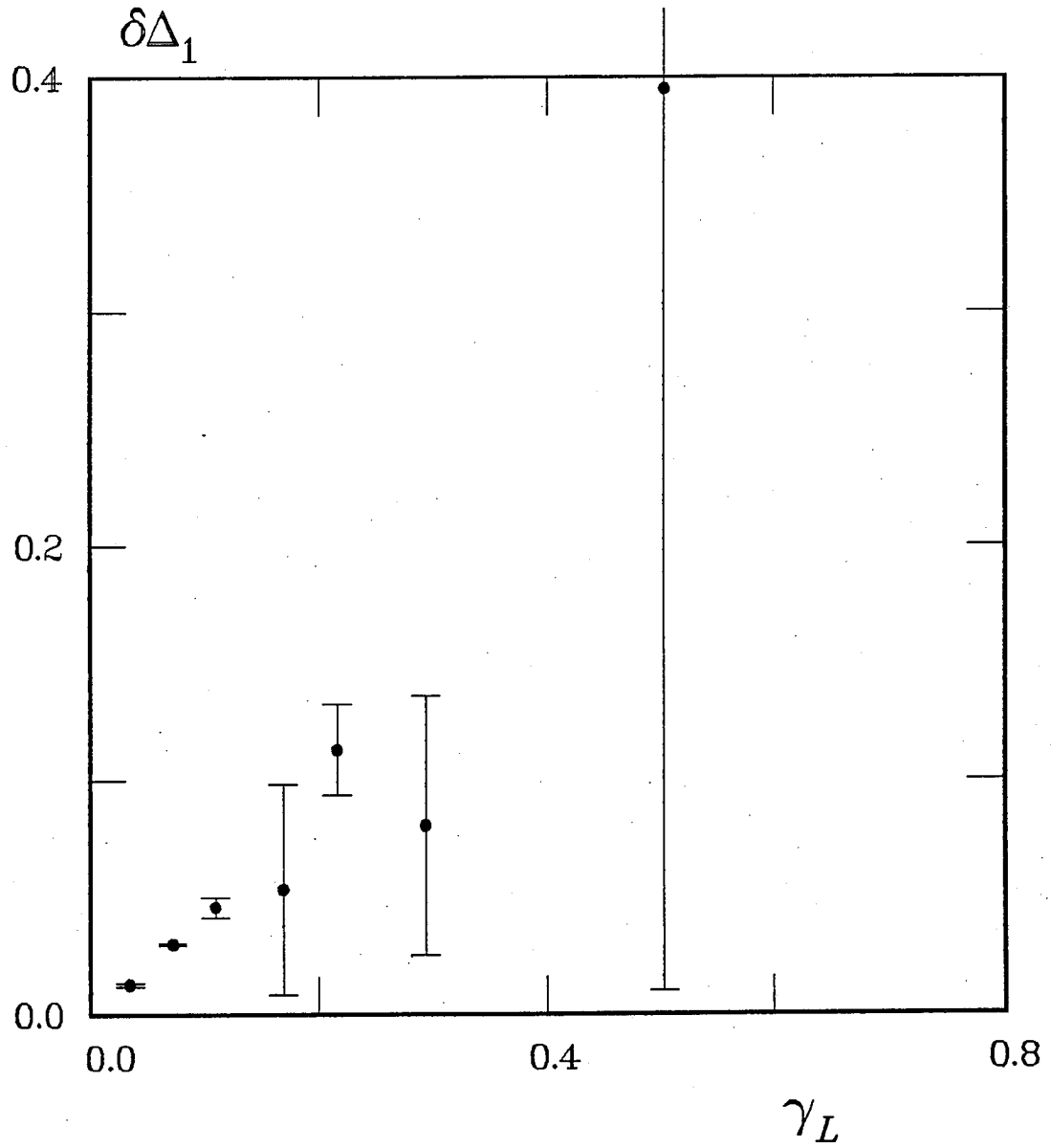

Fig. 12.

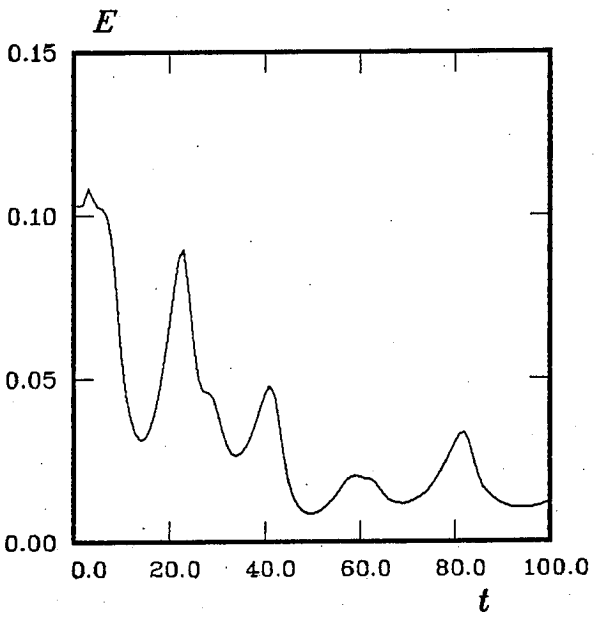
E
0.15
0.10
0.05
0.00
0.0
20.0
40.0
60.0
80.0
100.0
t

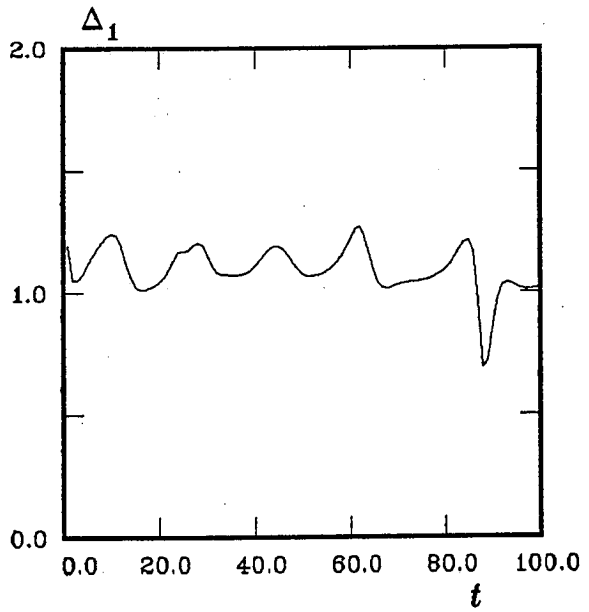
Δ1
2.0
1.0
0.0
0.0
20.0
40.0
60.0
80.0
100.0
t

Fig. 13.

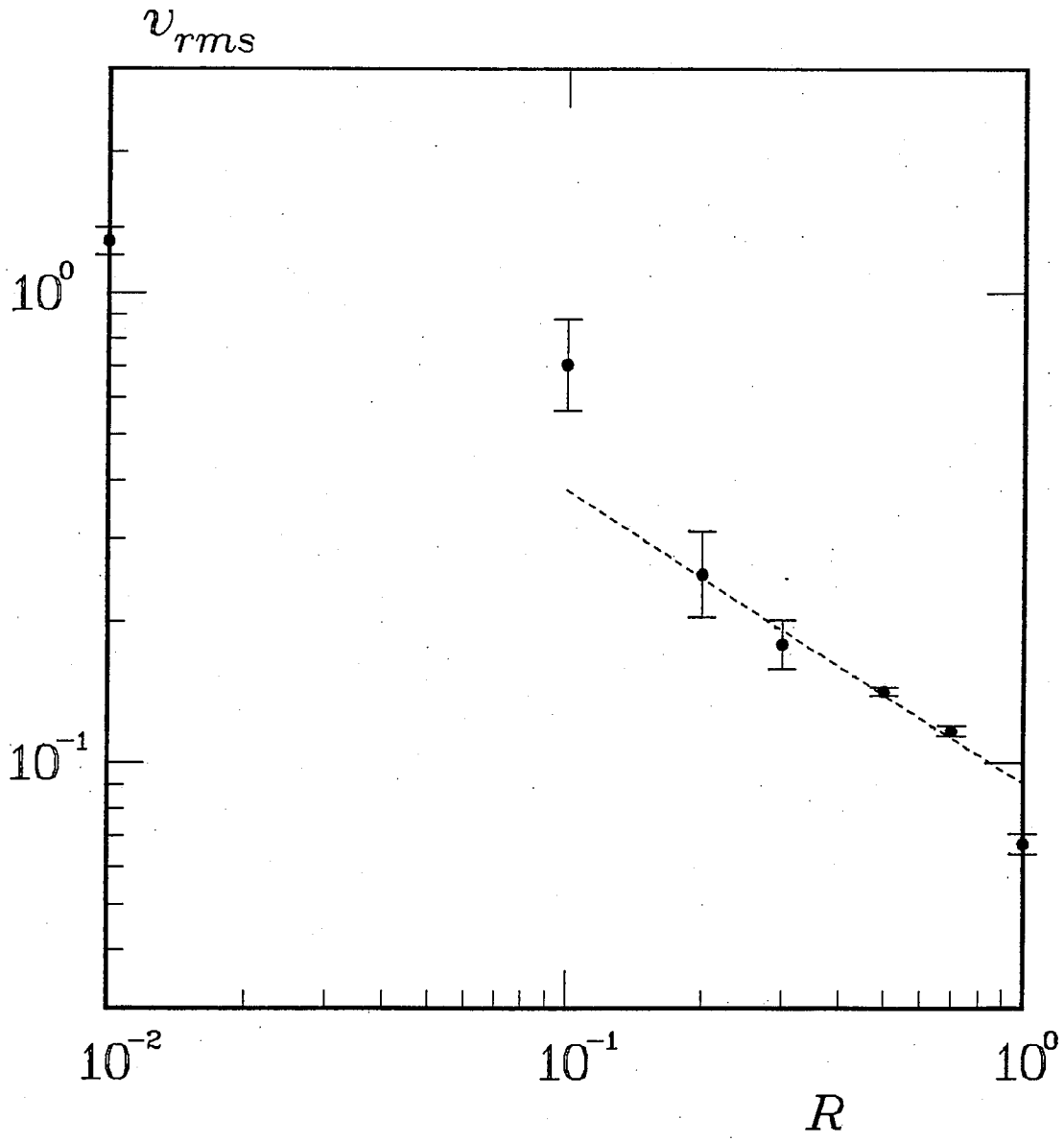

Fig. 14.